Retention of Delta Ferrite in the Heat-Affected Zone of Grade 91 Steel Dissimilar Metal Welds

MICHAEL W. KUPER and BOIAN T. ALEXANDROV

This study aimed to determine the mechanism of δ-ferrite retention in the coarse-grained HAZ (CGHAZ) of Grade 91 steel dissimilar metal welds (DMWs) with Ni-based filler metals. This phenomenon was investigated in four DMWs made with cold-wire gas tungsten arc process using Alloys 625, 617, 82, and P87 filler metals. A narrow band of δ-ferrite grains was identified in the CGHAZ in all welds. It was hypothesized that δ-ferrite retention was caused by local carbon depletion in the CGHAZ, which was validated through extensive thermodynamic and kinetic simulations and metallurgical characterization. Carbon diffusion across the fusion boundary was driven by the carbon chemical potential gradient between Grade 91 steel and the Ni-based filler metals, which was facilitated by long high-temperature dwell times resulting from a difference in heat capacity and thermal conductivity between the base and filler metals. A linear relationship was established between the amounts of retained δ ferrite and the predicted carbon depletion in the CGHAZ of each DMW. Alloy 625 filler metal generated the largest extent of carbon depletion and the most retained δ ferrite, followed by Alloys 617, 82, and P87. The carbon depletion resulted in local softening of the CGHAZ martensite.

https://doi.org/10.1007/s11661-019-05182-4

I. INTRODUCTION

CREEP strength-enhanced ferritic (CSEF) steels have been used extensively for pressure vessel components in fossil-fired and nuclear power plants. Among their desirable properties are adequate creep strength, ductility, corrosion resistance, cost, and weldability, which enable power generation with affordable infrastructure.[1,2] Efforts to maximize efficiency of the plants have resulted in raising operating temperatures, which has demanded use of creep-resistant stainless steels for the hottest regions of the plant including the primary fossil fired generators. However, Grade 91 steel is still used in the lower-temperature heat recovery steam generators of combined cycle power plants. In order to join the high- and low-temperature sections of these systems, dissimilar metal welds (DMWs) are necessary.

Early attempts to weld dissimilar steels using stainless steel filler metals resulted in extensive carbon migration near the fusion boundary that created brittle phases and large carbides, which weakened the welds and made them susceptible to cracking near the fusion boundary.[3,4] To help solve this problem, DMWs involving CSEF steels are now welded with Ni-based filler metals to reduce the driving force for carbon migration between the dissimilar steels used, which in turn, reduces the formation of hard and soft zones that weakened the creep strength of the welds.[5,6] However, the high concentration of carbide formers in the Ni-based alloys still creates a driving force for carbon migration toward the Ni-based filler metal, particularly during the mandatory postweld heat treatment (PWHT).[7–12] Premature failures near the fusion boundary in DMWs of 2.25-Cr 1-Mo steels have been attributed to carbon migration during PWHT from the CGHAZ into the partially mixed zone.[4,13–15]

In the case of Grade 91 steel DMWs with Ni-based filler metals specifically, the higher chromium content of the steel reduces the driving force for carbon migration, resulting in acceptable welds for industrial use with reduced carbon migration during the PHWT. However, premature failures near the phase boundary in such welds have been reported, although the exact failure mechanism is still unknown.[16] The challenge in identifying the root cause of failure is that the mechanism appears to be stochastic, with dependencies on fabrication history, joint design, operating conditions, and metallurgical factors including composition and grain size.[17] A phenomenon that may be related to the unexpected failures, retention of δ ferrite in the HAZ, was recently studied in Grade 91 steel DMWs.[18] δ ferrite in the HAZ of such welds was identified under the as-welded, heat-treated, and ex-service conditions.

MICHAEL W. KUPER and BOIAN T. ALEXANDROV are with the The Ohio State University, 1248 Arthur E Adams Dr., Columbus, OH, 43221. Contact e-mail: kuper.8@osu.edu
Manuscript submitted October 30, 2018.
Article published online April 5, 2019

Figure 1 shows the remnants of δ ferrite in a DMW that was removed from service because of premature failure at approximately 10 years. In contrast, due to the careful balance of austenite- and ferrite-stabilizing alloying elements, retention of δ ferrite is not typical for the HAZ of matching filler metal welds in this steel.

The presence of δ ferrite is significant because of its negative effect on creep strength and toughness.[19–24] For matching filler metal welds in high chromium martensitic steels, δ ferrite is most commonly found in the fusion zone after welding.[24–27] The mechanism for δ-ferrite formation in the fusion zone was determined to be partitioning of ferrite-stabilizing elements during solidification, which locally stabilized the δ-ferrite phase. Several studies have also been performed to predict if, and sometimes how much, δ ferrite will form based on the composition of the steel and accounting for the balance of ferrite- and austenite-stabilizing elements.[27–31] Other studies have indicated that the amount of δ ferrite present in the fusion zone of a susceptible material after welding may also be dependent on the heat input and weld thermal history, which influence the progress of phase transformations.[32,33] This mechanism, however, cannot explain the retention of δ ferrite in the HAZ of Grade 91 steel DMWs, since the HAZ remains solid and would therefore not experience partitioning caused by solidification. One possible mechanism for formation of residual δ ferrite could be carbon depletion of HAZ during welding. It has been shown that carbon acts as the strongest austenite-stabilizing element in high chromium martensitic steels[29,31] and a relatively small degree of variation in the carbon content is expected to have very strong effect on the phase balance in such steels.

The objective of this study is to identify the mechanism and the controlling factors for retention of δ ferrite in the HAZ of Grade 91 steel DMWs with Ni-based filler metals. Although retention of δ ferrite cannot be directly related to the reported service failures in such DMWs, identification of the related metallurgical phenomena could provide valuable insight into the overall failure mechanism.

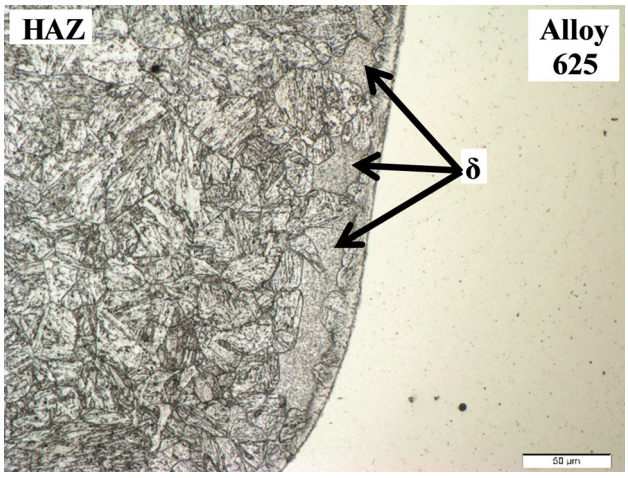

Fig. 1—Ex-service DMW (failed after 10 years in service) of Grade 91 steel with Alloy 625 filler metal containing δ-ferrite grains in the HAZ.

II. EXPERIMENTAL APPROACH

This study explores a hypothesis that retention of δ ferrite is caused by carbon depletion of the coarse-grained HAZ during welding as a result of the different chemical and thermophysical properties of Grade 91 steel and Ni-based filler metals. Bead on plate welding was performed with matching filler metal B91 and with a series of filler metals of Ni-based alloys 82, 625, 617, and P87 that are typically used in DMWs of Grade 91 steel to creep-resistant stainless steels. The welds were used to quantitate the filler metal effects on the HAZ thermal history and on the amount of retained δ ferrite. Thermodynamic and kinetic simulations were carried out to investigate the effect of filler metal composition on the behavior of carbon in the HAZ and the partially mixed zone during welding. The simulation results were validated with, and correlated to, the experimental results through metallurgical characterization.

A. *Test Welds*

HAZ δ ferrite was originally identified in multipass groove welds of Grade 91 steel pipes with Ni-based filler metals.[18] Such welds experience multiple reheats in the HAZ and partial re-melts in the fusion zone, resulting in complex thermomechanical histories and metallurgical phenomena that define the final weldment microstructure and properties. In order to isolate, identify, and quantitate the metallurgical phenomena leading to retention of HAZ δ ferrite, simplified "bead-on-plate"-type welds were investigated in this study. These welds would closely replicate the conditions for δ-ferrite retention in the first pass HAZ of multipass welds.

Test welds with Alloy 617, 82, and P87 Ni-based filler metals and B91 matching filler metal on Grade 91 steel substrate, together with an existing Alloy 625 DMW were included in this investigation. The chemical compositions of all materials are shown in Table I.

In order to obtain comparable results, all new welds were performed with the welding procedure of the Alloy 625 DMW as described in Reference 18. Longitudinal sections cut from a Grade 91 pipe with 6.5 in. outer diameter (OD) and 0.625 in. wall thickness were used as the base metal. Bead-on-plate welds oriented in parallel to the pipe longitudinal axis were made on the pipe OD surface using cold-wire gas tungsten arc welding (GTAW) process. The welding parameters are listed in Table II.

The thermal histories in the coarse-grained HAZ, where the δ-ferrite retention occurs, were measured using Type K thermocouples and recorded using data acquisition system at a sampling rate of 4 kHz. The thermocouples were installed by capacitor discharge welding in 2 mm holes drilled through the pipe inner diameter (ID) surface to varying distances from the fusion boundary. A picture of the welding setup can be seen in Figure 2. Recorded thermal histories with

Table I. Composition of the Grade 91 Base Material and Welding Filler Metals Used in This Study, Weight Percent

Alloy	C	Mn	Cu	Si	Ni	Cr	Mo	V	Al	Co	Nb	Fe
Grade 91	0.11	0.4	0.02	0.36	0.06	8.71	0.94	0.195	0.001	—	0.076	bal
B91	0.10	0.6	0.05	0.25	0.7	9	1	0.2	—	—	0.05	bal
625	0.02	0.1	0.01	0.14	bal	21.7	8.5	—	0.1	—	3.8	0.4
617	0.07	0.4	0.09	0.3	bal	22	8.7	—	1	12	—	0.3
82	0.04	2.8	0.03	0.09	bal	20	—	—	—	—	2.4	1.5
P87	0.10	1.5	—	0.3	bal	9	2	—	—	—	1	38

Table II. Welding Parameters

Filler Wire Process	None Autogenous GTAW	B91 Filler Metal Cold-wire GTAW	Ni-Based Filler Metals Cold-wire GTAW
Current (A)	190		
Voltage (V)	12 to 15		
Travel Speed (ipm)	3.6		
Arc Energy (kJ/in)	38		
Wire Feed Rate (ipm/cubic ipm)	—	35/0.056	57.9/0.056
Wire Diameter (in)	—	0.045	0.035

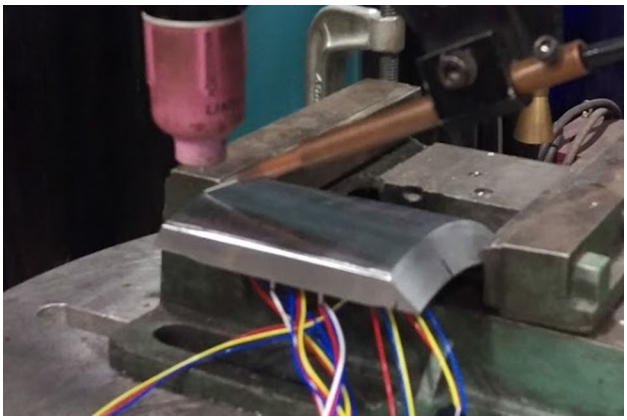

Fig. 2—The welding setup including the section of pipe used with thermocouples implanted into the bottom surface.

maximum temperatures corresponding to the coarse-grained HAZ were used in this study.

B. *Metallurgical Characterization*

All test welds were sectioned normal to the welding direction and prepared for metallurgical characterization using standard metallography procedures. A two-step procedure of 2 minutes etching with 20 pct nitric acid in water followed by 15 seconds immersion in Vilella's reagent was applied to reveal the microstructure of the Grade 91 steel side of the phase boundary.

The δ-ferrite content was quantitated using image-processing software. Light optical microscope (LOM) images were taken along the entire phase boundary of each weld. These were processed with MIPAR® to apply a contrast threshold for clear separation of the δ-ferrite grains from the martensitic matrix[34] and stitched together using Photoshop®. ImageJ® was used to measure the total δ-ferrite area and the length of the fusion boundary. The δ-ferrite area was then normalized by dividing by the length of the phase boundary. The normalized ferrite content has units of μm, and physically represents the average thickness (normal to the phase boundary) of the δ-ferrite band if the ferrite phase was a continuous band located adjacent to the phase boundary.

Vickers hardness testing was performed using an array of 750 indents with 50 μm spacing. The array was 15 indents wide normal to, and centered on the phase boundary, and 50 indents long parallel to the phase boundary. Indents were made using a 25 g load. Hardness values were categorized based on the location and microconstituent (ferrite or martensite) in which the corresponding indent was located and plotted *vs* their proximity to the phase boundary. This analysis was only performed for the DMWs made with Alloy 625 and P87 filler metals because it was predicted that the HAZ of these welds would have, correspondingly, the highest and lowest level of carbon depletion.

The chemical composition of δ ferrite and martensite microstructural constituents in a DMW with Alloy 625 filler metal were quantitated and compared through compositional line scans using EPMA within an SEM. Two parallel sets of line scans were performed, with one normal to, and one parallel to the phase boundary. For each pair of lines, one intersected a δ-ferrite grain while the other measured only martensite grains. Comparison of the line scans was aimed to identify potential compositional gradients and/or variations.

Chromium equivalents, experimentally developed for predicting the presence of δ ferrite in high chromium

martensitic steels[27–31] were used to predict the maximum carbon content and the minimum level of carbon depletion for retention of δ ferrite in the tested heat of Grade 91 steel.

C. *Thermodynamic and Kinetic Simulations*

1. *Solidification temperature ranges and chemical potential gradients*

Thermo-Calc® with the TCFE9 and TCNI8 databases was used to estimate the solidification temperature ranges for the alloys in this study using the modified Scheil-Gulliver Equation.[35] This equation assumes no diffusion in solid phases, infinitely fast diffusion in liquid phases, and equilibrium at the solid–liquid interface. In this case, the simulation was modified to allow for partial redistribution of carbon in the solid because of its fast diffusing nature.

Thermo-Calc® with the TCFE9 and TCNI8 databases was used to compute chemical potentials for carbon. The carbon chemical potential gradient was then calculated as a function of temperature by subtracting the carbon chemical potential of Grade 91 steel from the filler metal carbon chemical potential. Because the chemical potentials used for the calculation were computed using the individual alloys in their pure forms, the calculated gradient does not account for dilution, the width of the transition zone, or nonequilibrium conditions. The resulting curves will therefore be an overestimate of chemical potential gradient, but the differences between chemical potential gradients from the various alloys used will be directly comparable.

The simplifications made to determine the magnitudes of the chemical potential gradients were accounted for by creating a diffusion model that incorporated the spatial chemical profiles present in the actual physical DMWs.

2. *The diffusion model*

Computational modeling *via* the CALPHAD method was used to explain the observed δ ferrite in the CGHAZ of DMWs. A model was developed using DICTRA® to predict the compositional profile across a dissimilar metal weld.[36] The model was created using two cells containing the HAZ and fusion zone chemistries respectively as they existed at the Grade 91 steel solidus temperature. Figure 3 shows the initial setup of the model including the geometry and the composition profile for the Alloy 625 weld as a function of dilution. The initial composition profile in the HAZ cell was defined as the Grade 91 steel composition. The composition profile in the fusion zone cell was estimated using the error function based on the dilution profile of all elements except carbon, measured on a weldment using energy dispersive spectroscopy (EDS). Since the diffusion of slower diffusing elements was assumed negligible during the weld thermal cycle, the measured composition profile after welding accounts for mechanical mixing alone. As such, the measured dilution profile was assumed appropriate for use as the starting profile for all elements, including carbon. With respect to the composition, the model accounts for the seven most influential alloying elements: Fe, C, Cr, Mo, Mn, Nb, Ni (and Co in the case of Alloy 617).

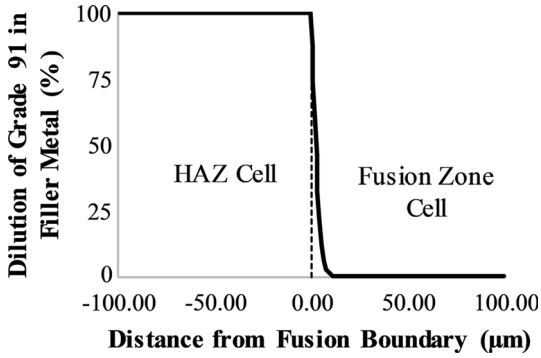

Fig. 3—A schematic of the initial chemical profile (based on dilution) of the cells comprising the DICTRA® model.

Once the initial composition profile was set, the thermal path was defined. Figure 4 shows the cooling curve measured in the Alloy 625 DMW weld pool measured by plunging a Type C thermocouple into the weld pool during welding, based on data from Reference 18. The cooling curve was fitted to two polynomials, each containing a portion of the data, which were used to define the thermal cycle. 1450 °C was chosen as a maximum temperature because it corresponds approximately to the solidus temperature for Grade 91 steel. This temperature is also appropriate for the compositional profile used, which was based on the estimated solid–liquid interface at the fusion boundary during welding.

The simulation was performed using high-temperature and low-temperature segments. The low-temperature segment ($T < 1100$ °C) incorporated the following phases/crystal structures: face-centered cubic (FCC), body-centered cubic (BCC), $M_{23}C_6$ carbides, and MX carbonitrides. The high-temperature segment ($1450 > T > 750$ °C) contained the liquid, FCC, and BCC phases, but not the carbides or carbonitrides. For the high-temperature segment, including precipitates in the presence of the liquid phase caused convergence errors, so diffusion was computed without including them. The low-temperature segment was computed using the extracted results at 1100 °C (after fusion zone solidification but before the onset of precipitation) from the high-temperature segment. Afterward, the overlaps in the high-temperature and low-temperature segments were compared, revealing no differences until the onset of precipitation. Once precipitation began, the results from the low-temperature segment were used.

The developed model predicts the evolution of the composition profile, phase balance, and precipitation across the HAZ and fusion zone during cooling from 1450 °C following the experimentally measured cooling curve.

D. *Assumptions of the Diffusion Model*

The model makes a few assumptions, which merit discussion. First, the model assumes a fixed phase boundary between the two cells. While diffusion can occur between the two cells, the location of the initial

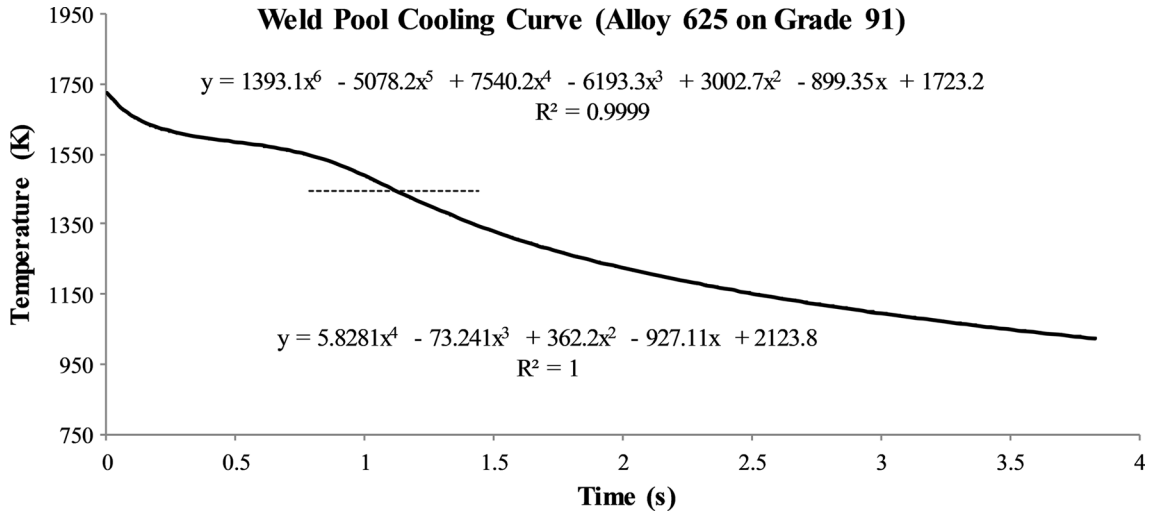

Fig. 4—Cooling curve measured using a thermocouple plunge into the fusion zone of the Alloy 625 DMW (data from Ref. [18]). The curve has been divided into two sections, each fitted with a polynomial to maximize the accuracy of the functions used compared with the data.

interface cannot move. In reality, the local composition changes that occur during cooling will influence the phase stability at a given node, which would result in a moving phase boundary. Based on the small diffusion distance during the simulation, this assumption should not significantly affect the results. Second, the homogenization mode used in the model assumes instantaneous phase transformations based on the equilibrium phase diagram. Therefore, on cooling, the model will predict a phase change once a boundary is reached on the equilibrium phase diagram specific to a given node's composition. In reality, kinetic factors can delay phase transformations creating depressions in the phase transformation temperatures. The homogenization mode in DICTRA® does not account for this phenomenon. Finally, the thermal histories used for the array of simulations were all the same, corresponding to the measured thermal history from the Grade 91 steel/Alloy 625 weld. While in reality the weld cooling rate would vary based on the filler metal composition, the Ni-based filler metals have similar thermophysical properties, making the potential error from this assumption insignificant.

III. RESULTS

A. *Thermal Histories in the HAZ*

The measured thermal history in the CGHAZ of the Grade 91 steel weld made with B91 filler metal is shown in Figure 5 along with previously measured thermal histories in Grade 91 autogenous and Alloy 625 filler metal welds.[18] The peak temperatures, the heating and cooling rates and times, and the total dwell time of HAZ spent above 1000 °C for all three welds are shown in Table III.

B. *Metallurgical Characterization*

The B91 filler metal weld exhibited the typical microstructure for Grade 91 steel welds, consisting of fresh martensite in the HAZ, shown in Figure 6. The

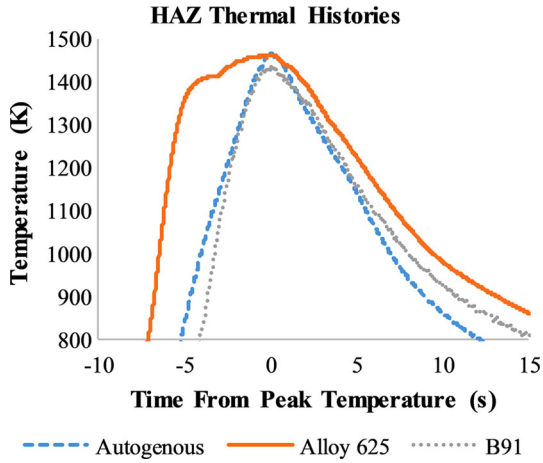

Fig. 5—Thermal histories measured inside the HAZ of bead on plate welds made on Grade 91 steel. Data for the autogenous and 625 filler metal curves are adopted from Ref. [18].

DMWs, however, all contained δ-ferrite grains as an additional microconstituent, which can be seen in Figure 8. These δ-ferrite grains were located in the HAZ, forming a semicontinuous chain that was separated by approximately 20 to 40 μm from the dissimilar interface.

Macrographs of each DMW can be seen in Figure 7, which shows the profiles of the welds. The complex shape was related to a combination of eddy currents and convection within the molten weld pool, as well as the interaction between the high-temperature weld pool and the room-temperature filler metal being added.

The size, distribution, and area fraction of the δ-ferrite grains varied based on filler metal selection and location within the weld. Figure 8 shows the qualitative difference of the δ-ferrite distribution in the root area of each weld. The width of δ-ferrite grains (normal to the dissimilar interface) was the largest at the weld roots and the smallest at the weld toes, Figure 9.

Table III. Peak Temperatures, Heating/Cooling Rates and Times, and Total Time Spent Above 1000 °C in the HAZ of Each Weld

		Heating		Cooling		
Filler Metal	Peak Temp (°C)	Time (s)	Rate (°C/s)	Time (s)	Rate (°C/s)	Total Time (s)
Autogenous	1190	2.00	95.23	2.96	64.19	4.96
B91	1155	1.70	91.18	3.35	46.27	5.05
Alloy 625	1188	5.64	33.38	4.53	41.49	10.17

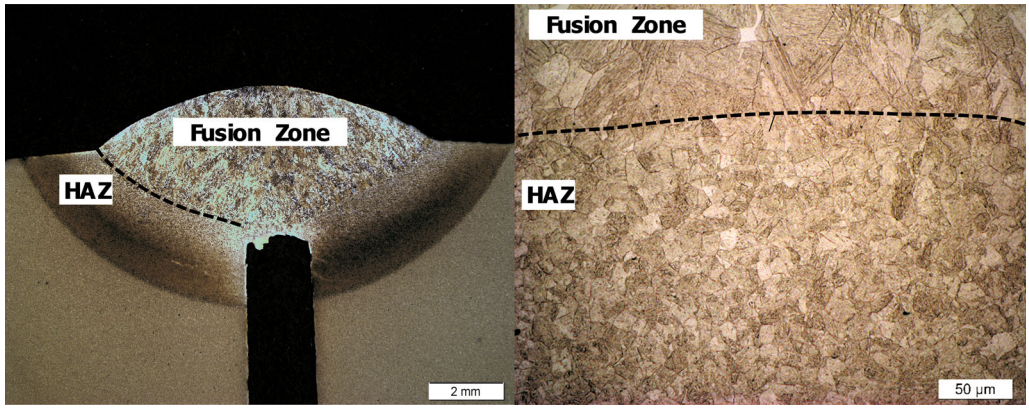

Fig. 6—B91 weld showing the fusion and heat-affected zones (left), and a close-up of the fusion boundary (right), each with the approximate location of the fusion boundary. The hole below the weld nugget in the left image was a predrilled hole, which housed a thermocouple during welding.

For each DMW, the total surface area of δ-ferrite grains was quantitated and normalized based on (divided by) the length of the fusion boundary, Figure 9 and Table IV. The highest normalized δ-ferrite content was found in the HAZ of the Alloy 625 filler metal weld, followed by Alloy 617, 82, and P87 filler metal welds.

A section of the developed DMW hardness maps is shown in Figure 10. The hardness indents of these maps were grouped by microstructural constituents as follows: HAZ martensite, ferrite band martensite, ferrite band ferrite, and fusion zone austenite. The hardness distribution was plotted as a function of distance from the phase boundary and color coded based on microconstituents, Figure 11. Indents located in more than one microconstituent were discounted from the analysis. For the HAZ in both Alloy 625 and P87 filler metal welds, the HAZ martensite had the highest hardness followed by the ferrite band martensite, and the ferrite band ferrite, Table V. With better than 99.9 pct confidence, two-tailed t-tests indicated that the HAZ microconstituents in each weld have statistically distinct hardness. In addition, a separate statistical test indicated a 99.6 pct confidence index that the hardness of ferrite band martensite in the welds with Alloy 625 and P87 was also statistically distinct.

Figure 12 shows the location of the EPMA line scans in the CGHAZ of the P87 filler metal weld. Two sets of line scans were performed, one oriented parallel and one normal to the fusion boundary. One line of each set crossed through the martensitic microstructure only, while the other one crossed a single δ-ferrite grain. The EPMA profiles showed no difference in the distributions of ferrite- and austenite-stabilizing elements between the martensite and δ-ferrite microconstituents locally, though a slight elevation in the Ni concentration was found in the HAZ immediately adjacent to the phase boundary, Figure 13. Each set of lines was compared using the matched pairs' confidence intervals for each alloying element except carbon. The 95 pct confidence intervals show that each pair of line scans was statistically indistinguishable from one another, Table VI. The maximum effect of compositional variability on the Cr equivalent was calculated based on the equation from an equation published in Reference 27 using the extreme compositional limits that produced the highest and lowest Cr equivalents. These limits can also be found in Table VI.

The carbon distribution map and line scans produced using EPMA were not reported here since the signal-to-noise ratio was too low to detect any measureable change. Therefore, it was necessary to predict the carbon profiles using thermodynamic and kinetic simulations.

C. *Thermodynamic and Kinetic Modeling of Carbon Diffusion During Welding*

The equilibrium and nonequilibrium liquidus and solidus temperatures based on the Scheil-Gulliver simulation for the alloys used in this study can be found in Table VII along with their solidification temperature ranges.

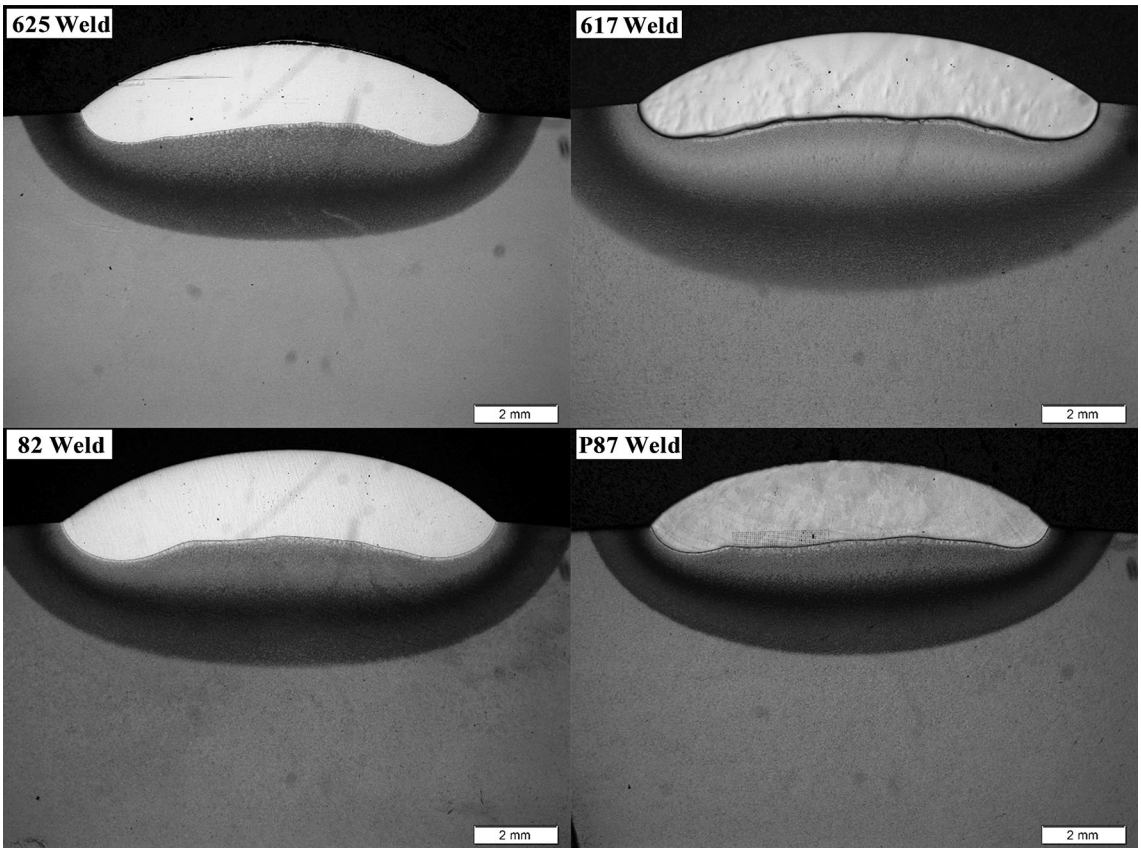

Fig. 7—Macrographs showing the weld bead profiles for the DMWs.

The predicted maximum gradients of the chemical potential for carbon between Grade 91 steel and each of the filler metals were plotted as a function of temperature, Figure 14. The carbon chemical potential gradient in the B91 filler metal weld remained close to zero throughout the range from 1600 °C to room temperature, indicating absence of driving force for carbon diffusion. In the Alloy 625 weld, the carbon chemical potential gradient was strongly negative above 600 °C, providing condition for carbon diffusion from the HAZ into the austenitic fusion zone. The gradients in the Alloy 617, 82, and P87 welds contained both positive and negative regions, providing conditions for carbon diffusion in both directions across the phase boundary, depending on the corresponding temperature ranges.

The diffusion model described in Section II–C–2 was applied to predict the behavior of carbon in the HAZ and fusion zone of all studied DMWs. Extensive carbon redistribution was predicted to occur on cooling between 1450 °C and 700 °C, Figure 15. Below 700 °C, the predicted carbon profiles in all welds did not change significantly, with concentration values differing by less than 1 pct of the concentration at 700 °C. Significant carbon depletion in the HAZ of the Alloy 617, 82, and P87 welds was predicted to occur during cooling from 1450 °C to 1350 °C. This was followed by reversed carbon diffusion between 1350 °C and 700 °C that partially compensated the carbon depletion in the HAZ of Alloy 617 and 82 welds. The predicted reversed diffusion in the Alloy P87 weld resulted in carbon accumulation in the HAZ. The Alloy 625 weld was predicted to undergo carbon depletion throughout the entire 1450 °C to 700 °C temperature range, resulting in the most significantly depleted HAZ.

The predicted temperature dependences of the average and minimum carbon concentrations in the HAZ of all welds are shown in Figure 15. The average carbon concentrations were calculated by integrating the predicted carbon content in the portion of the HAZ affected by carbon diffusion (having a different concentration than the base metal) and dividing by the width of that region. By integrating over this region, the calculation removed any bias that might be created from choosing the cell size in the model. A schematic of this calculation and the resulting average carbon contents are shown in Figure 16 and Table VIII correspondingly. The minimum and average carbon concentrations in the HAZ are presented in Figure 17 and, which show that Alloy 625 filler metal produces the largest HAZ carbon depletion in Grade 91 steel DMWs, followed by Alloys 617, 82, and P87. Additionally, Figure 17 includes the average equilibrium solidification temperatures for the Ni-based filler metals.

The minimum carbon concentrations were tracked at a location approximately 25 μm away from the initial dissimilar interface that corresponded to the microstructural region containing δ-ferrite grains. The local minima in carbon concentration were plotted on top of the

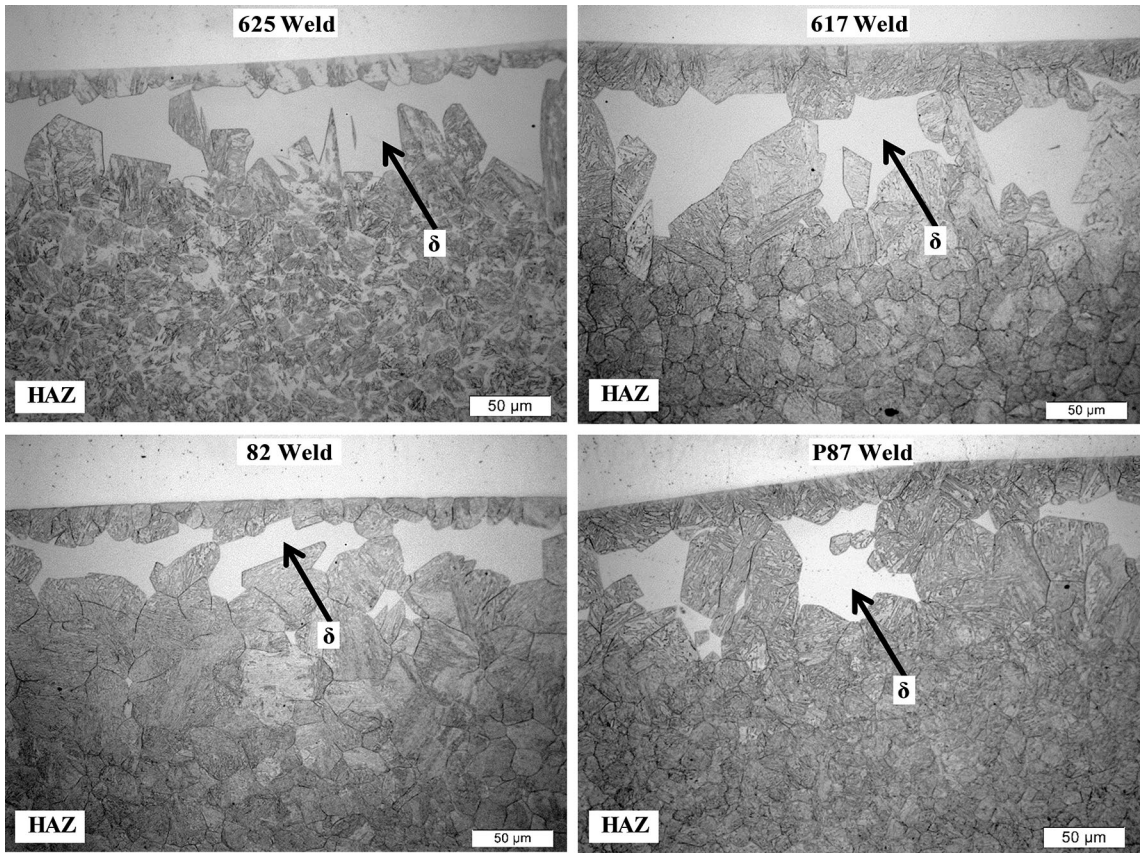

Fig. 8—Images near the fusion boundary in the various DWMs showing the δ-ferrite grains in the HAZ. Images were taken near the weld roots.

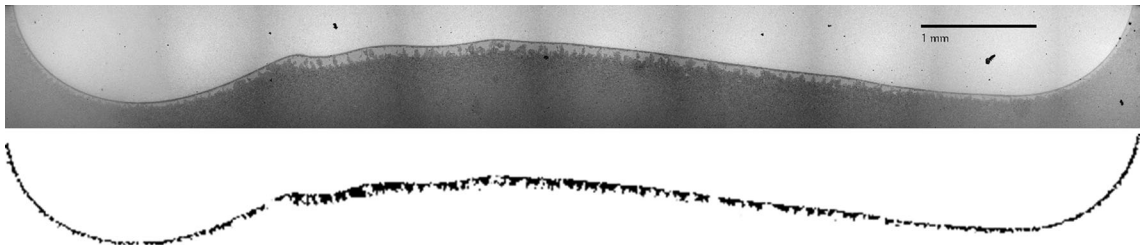

Fig. 9—Stitched (top) and processed (bottom) image of δ ferrite in the HAZ of the Alloy 625 DMW used for quantitative analysis.

Table VI. Total and Normalized δ Ferrite Areas in the HAZ of Alloys 625, 617, 82, and EPRI P87 Welds

Alloy	Total Ferrite Area (mm^2)	Normalized Ferrite Band Width (μm)
625	0.348	30.24
617	0.449	25.53
82	0.247	22.12
P87	0.119	11.37

equilibrium pseudo-binary phase diagram for carbon in Grade 91 steel that is shown in Figure 18. For all filler metals, the maximum extent of HAZ carbon depletion coincides with temperature range of stable δ ferrite in Grade 91 steel. Calculations based on experimentally developed chromium equivalent equations,[27–31] were used to determine the threshold below which δ ferrite would be present, Table IX. The average of the threshold values, 0.08 wt pct was plotted on the Grade 91 phase diagram, Figure 18.

The normalized δ-ferrite content shown in Table IV was plotted against the predicted average carbon concentration in the portion of the HAZ affected by carbon diffusion as shown in Figure 19. A very strong linear dependence, with a correlation coefficient of 0.99, was found between the δ-ferrite content and the predicted HAZ carbon concentration.

IV. DISCUSSION

This study has shown that, in contrast with matching filler metal welds, utilization of Ni-based filler metals in Grade 91 steel DMWs can result in retention of δ-ferrite grains in the coarse-grained HAZ, Figure 6 and Figure 8. It was experimentally proven that: (1) the amount of retained δ ferrite is filler metal specific, Table IV, (2) the δ-ferrite and martensite constituents in HAZ have indistinguishable contents of ferrite- and austenite-stabilizing alloying elements, Table VI and Figure 13, (3) the martensitic constituent in the δ-ferrite band is softer compared to the rest of HAZ martensite, and (4) the hardness of the δ-ferrite band martensite is also filler metal specific, Figure 11 and Table V.

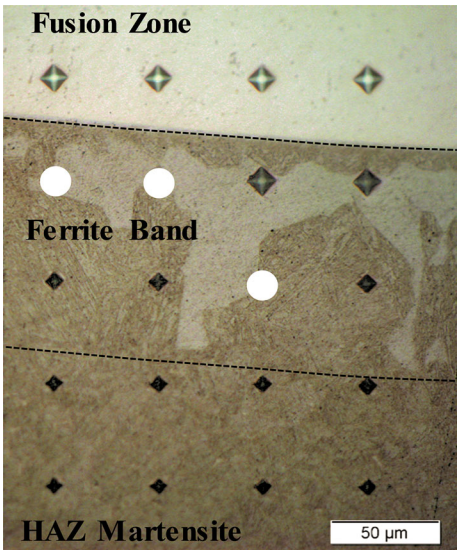

Fig. 10—Example of a hardness map from the Alloy 625 weld indicating the microstructural weld regions. The white circles indicate measurements that were not used because the indent was located on a border between phases.

The experimental results of this study provided supporting evidence to the hypothesis that retention of δ ferrite in the HAZ of Grade 91 DMWs with Ni-based filler metals was caused by the differences in the chemical and thermophysical properties of these materials that lead to local carbon depletion in the coarse-grained HAZ. However, a direct evidence of carbon depletion in the HAZ could not be established due to limited sensitivity and/or low spatial resolution for small variations in carbon concentration of the available characterization tools, including EPMA. This lead to utilization of thermodynamic and kinetic simulations to study the behavior of carbon in the HAZ and partially mixed zone during welding. The simulation results were validated with and correlated to the results of the performed metallurgical characterization.

A. *Carbon Behavior During Welding in Grade 91 DMWs*

1. *Controlling factors*

The significant differences in compositional and thermophysical properties of Grade 91 steel and Ni-based filler metals resulted in longer dwell of HAZ in the temperature range of stable δ ferrite, active

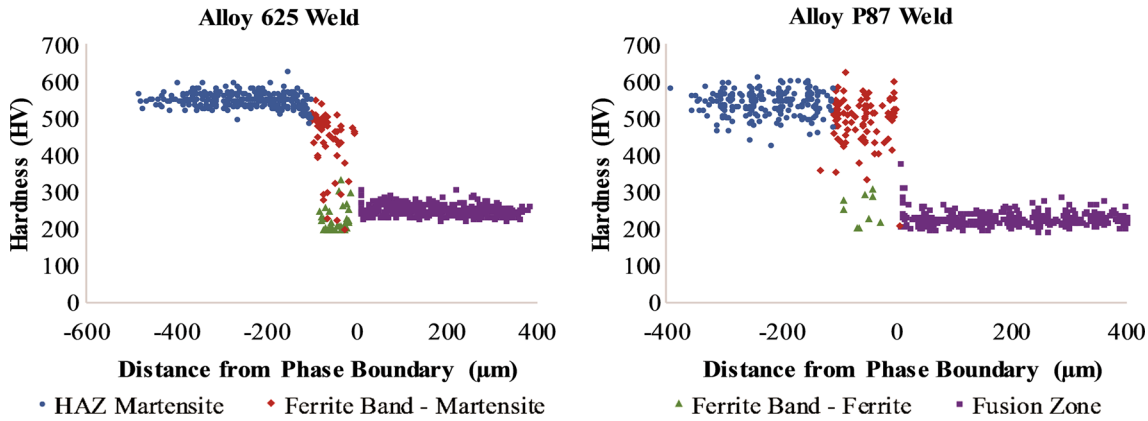

Fig. 11—Distribution of hardness values as a function of distance from the phase boundary, categorized by regions and microstructural constituents for the welds with Alloy 625 (left) and P87 (right) filler metals.

Table V. Average Hardness with 95 Pct Confidence Intervals for Microstructural Constituents in the Alloy 625 and P87 Welds

	Alloy 625 Weld		P87 Weld	
	Mean ($HV_{0.025}$)	95 Pct CI (HV)	Mean ($HV_{0.025}$)	95 Pct CI (HV)
HAZ Martensite	553	± 3.2	548	± 4.4
Ferrite Band—Martensite	445	± 7.2	500	± 12.3
Ferrite Band—Ferrite	223	± 9.4	226	± 12.0
Fusion Zone	253	± 3.1	225	± 1.9

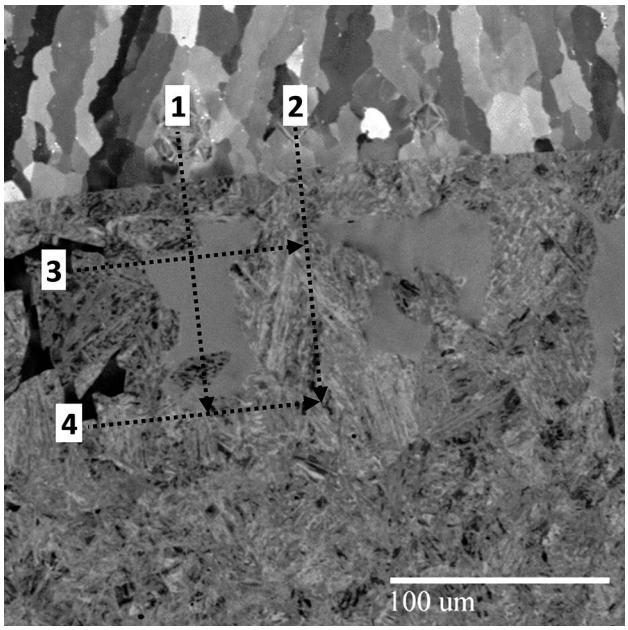

Fig. 12—SEM micrograph taken at the fusion boundary of Grade 91 steel welded with Alloy P87. The dashed lines indicate the locations of the EPMA traverses. Lines 1 and 3 intersect a ferrite grain while Lines 2 and 4 do not.

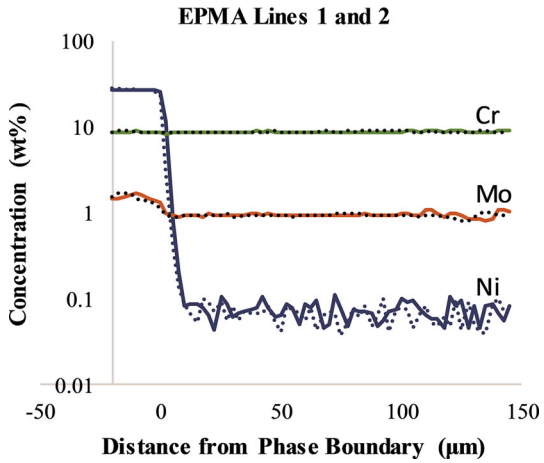

Fig. 13—Results from EPMA including the Line 1 and Line 2 concentration profiles for iron, nickel, and chromium from the Alloy P87 weld.

carbide dissolution, and significant carbon chemical potential gradients, which generated conditions for carbon migration across the dissimilar phase boundary.

The use of a Ni-based filler metal in Grade 91 steel welds created carbon chemical potential gradients across the dissimilar fusion boundary. These gradients predicted the driving force for carbon migration with magnitudes that varied with temperature and were specific to each of the selected filler metals, Figure 14. The carbon chemical potential gradients generated by the tested alloys can be related to the combined content of carbide formers: chromium, molybdenum, and niobium, Table I. Alloy 625 created a strongly negative carbon chemical potential gradient at the fusion boundary throughout the temperature ranges of solidification in the partially mixed zone, which when coupled with carbide dissolution, resulted in the formation of δ ferrite in the HAZ. The lower combined content of carbide formers in Alloys 617, 82, and P87 resulted in a transition from relatively less negative to positive carbon chemical potential gradients in the temperature range of extensive carbon migration, indicating conditions for reverse diffusion across the dissimilar fusion boundary. Based on the chemical potential gradient plots in Figure 14, it can be concluded that Alloy 625 would provide conditions for the highest degree of carbon depletion and retention of δ ferrite in the HAZ, followed by Alloys 617, 82, and P87. Such ranking of the effect of filler metal composition corresponds to the measured HAZ δ-ferrite content in welds with these alloys, Table IV.

Thermodynamic simulations have shown that the solidification temperature range of Ni-based filler metals overlaps with the temperature range of stable δ ferrite in Grade 91 steel.[18] The latent heat of fusion released by the Ni-based filler metal, in combination with its lower thermal conductivity, was expected to extend the dwell time in the temperature range of stable δ ferrite in the Grade 91 steel HAZ. This effect was experimentally proven in Reference 18 and in this study by acquiring HAZ thermal histories in autogenous, matching, and DMWs, Figure 5 and Table III. The HAZ in the autogenous and B91 filler metal welds both had similar heating rates, cooling rates, and high-temperature dwell times, which contrasted to the weld with Alloy 625, Table III. In fact, the Alloy 625 weld HAZ remained above 1000 °C for more than twice as long compared to the autogenous and matching filler metal welds. The significance of the longer high-temperature dwell time is related to its potential effect on carbides dissolution, carbon depletion of the HAZ, and δ-ferrite stability.

The significant differences in solidification temperature ranges between Grade 91 steel and Ni-based filler metals resulted in a wide solidification temperature range across the partially mixed zone. The solidus temperatures of the Ni-based filler metals varied between 1132 °C and 1290 °C, Table VII, which was between 215 °C and 373 °C below the liquidus temperature for Grade 91 steel. Therefore, presence of liquid in the partially mixed zone of the DMWs would partially overlap the stable δ-ferrite region of the Grade 91 steel equilibrium phase diagram.[18] Based on the DICTRA simulation results, Figures 15 and 17, the most significant carbon migration occurred in the temperature range corresponding to solidification of the fusion zone. Diffusion in this range occurred at a more rapid rate for two reasons. First, there was a strong driving force for carbon diffusion, which was enabled by the high temperatures of this range. Second, high diffusion rates in the liquid phase and mechanical mixing of the weld pool would help to homogenize the added carbon from the HAZ, meaning there would be little reduction in the carbon chemical potential gradient across the solid–liquid boundary. Carbon depletion in the HAZ at high temperatures would stabilize δ-ferrite regions and

Table VI. 95 Pct Confidence Intervals for the Mean Differences in the Measured Elements Between Pairs of EPMA Line Scans in the Alloy P87 Weld

	Lines 1 and 2		Lines 3 and 4	
Element	Lower Mean	Upper Mean	Lower Mean	Upper Mean
Cr	− 0.0584	0.0048	− 0.0144	0.0547
Mn	− 0.0126	0.0082	− 0.0020	0.0171
Mo	− 0.0060	0.0388	− 0.0257	0.0059
Nb	− 0.0183	0.1251	− 0.0058	0.0018
Ni	− 0.0276	0.0682	− 0.0113	0.0106
Si	− 0.0056	0.0049	− 0.0056	0.0044
V	− 0.0010	0.0079	− 0.0058	0.0025

Table VII. The Liquidus and Solidus Temperatures of the Alloys Used in This Study, Along with Their Solidification Temperature Range

Alloy	Equilibrium/Scheil Liquidus Temperature (°C)	Equilibrium Solidus Temperature (°C)	Scheil Solidus Temperature (°C)	Scheil Solidification Temperature Range (°C)
625	1364	1305	1132	232
617	1397	1337	1235	162
82	1380	1328	1218	162
P87	1396	1354	1290	106

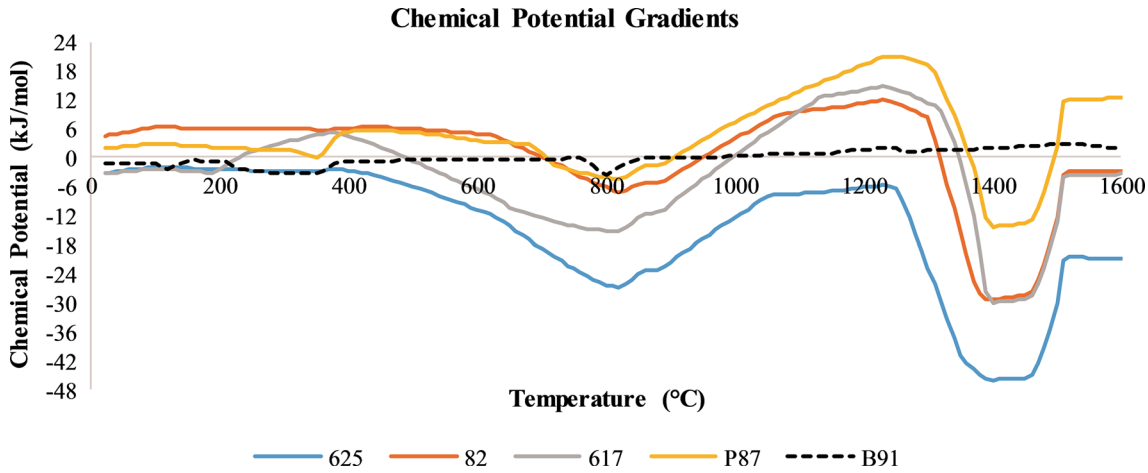

Fig. 14—Chemical potential gradients between various filler metals and Grade 91 steel as a function of temperature.

locally lower the phase transformation temperature from δ ferrite to austenite, which resulted in retention of δ ferrite at room temperature. There was a strong correlation of the extent of predicted carbon depletion (Figures 13 and 15) and the amount of retained δ ferrite (Figures 5 and Table IV) with the solidification temperature ranges of the Ni-based filler metals (Table VII). Alloy 625, with the widest solidification temperature range, generated the highest degree of carbon depletion and δ-ferrite retention, and Alloy P87, which had the narrowest solidification temperature range, generated the least carbon depletion and δ-ferrite retention.

Analysis of the kinetics of carbide dissolution has shown that the dwell time of the HAZ in Ni-based filler metal welds would be sufficient for complete dissolution of $M_{23}C_6$ carbides.[18] The dissolution of $M_{23}C_6$ carbides would provide free carbon for diffusion across the partially mixed zone, driven by the strong chemical potential gradient between the Grade 91 HAZ and a Ni-based filler metal, Figure 14. Carbides in Grade 91 steel are rich in ferrite stabilizers, mainly Cr, and are primarily located at prior austenite grain boundaries and martensite lath boundaries. Therefore, their dissolution would result in local

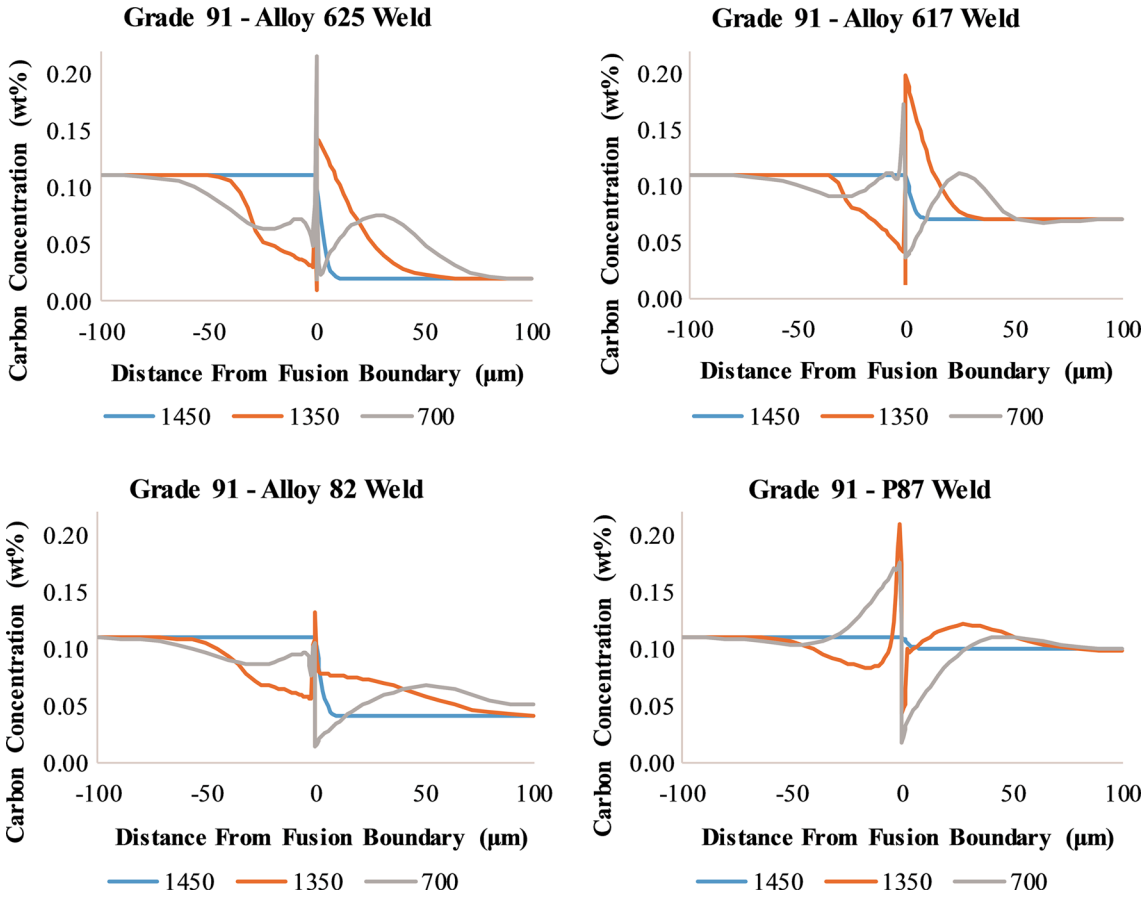

Fig. 15—Predicted carbon chemical profiles for various DMWs at various temperatures during cooling.

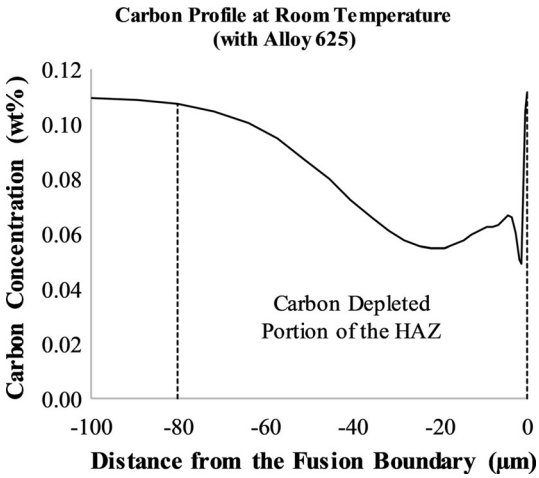

Fig. 16—A schematic of the procedure for averaging the predicted carbon content in the region of the HAZ affected by carbon diffusion.

enrichment in ferrite-stabilizing elements, providing easy nucleation sites for δ ferrite.

The longer dwell times at high temperatures in DMWs would facilitate more extensive carbide dissolution in the coarse-grained HAZ and a greater extent of diffusion controlled δ-ferrite transformation. Carbon diffusion rates in δ ferrite are higher than in austenite,[37,38] meaning that the higher δ-ferrite content in the HAZ of DMWs would provide for a greater extent of carbon mobility as compared with an austenite matrix. The presence of a strong chemical potential gradient in combination with longer dwell times in the temperature range of stable δ ferrite would result in carbon depletion of the HAZ in DMWs. The carbon depleted δ ferrite in DMWs would be stabilized and could remain untransformed, resulting in retained δ ferrite on cooling to room temperature, as shown in Figures 8 and 9. Due to the absence of driving force for carbon depletion in the HAZ of matching filler metal welds, the balance of austenite- and ferrite-stabilizing alloying elements in the HAZ δ ferrite is preserved, and on cooling, the HAZ δ ferrite would subsequently transforms to austenite, then martensite once the martensite start temperature was reached, Figure 6.

2. *Carbon depletion in HAZ*

The kinetic simulations performed in this study predicted significant carbon depletion in the HAZ of Grade 91 steel DMWs, Figures 14 and 15, which was strongly affected by the nickel base filler metal composition and the related chemical potential gradients across the dissimilar fusion boundary, Figure 14. Alloy 625 generated the highest predicted level of HAZ carbon depletion, followed by Alloys 617, 82, and P87. Some degree of HAZ carbon content reversion in Alloy 617

Table VIII. Predicted Average Carbon Concentration in the Diffusion-Affected Portion of the HAZ for Welds Using Alloys 625, 617, 82, and EPRI P87 on Grade 91 Steel

Alloy	Average Carbon Concentration in the HAZ (Wt Pct)
625	0.0814
617	0.0938
82	0.0963
P87	0.1181

and 82 welds and carbon accumulation in the Alloy P87 weld was predicted to occur next to the fusion boundary in the lower-temperature range of active carbon migration, between approximately 1300 °C and 900 °C based on Figure 14. This effect can be related to the positive chemical potentials, generating conditions for reverse carbon diffusion in these welds within the corresponding temperature range. Due to limited sensitivity for low-carbon concentrations of existing characterization techniques, direct evidence of HAZ carbon depletion in Grade 91 DMWs could not be provided in this study.

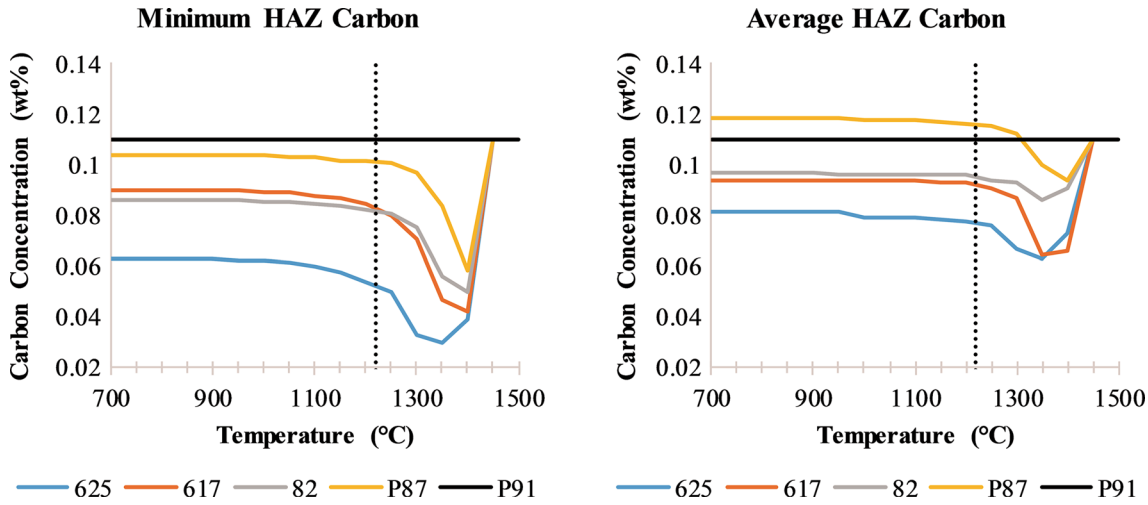

Fig. 17—Predicted minimum carbon content in the HAZ (left) and the average carbon content in the HAZ (right) for each simulated weld as a function of temperature during cooling. The vertical dotted line indicates the average equilibrium solidification temperature for the Ni-based alloys used in this study.

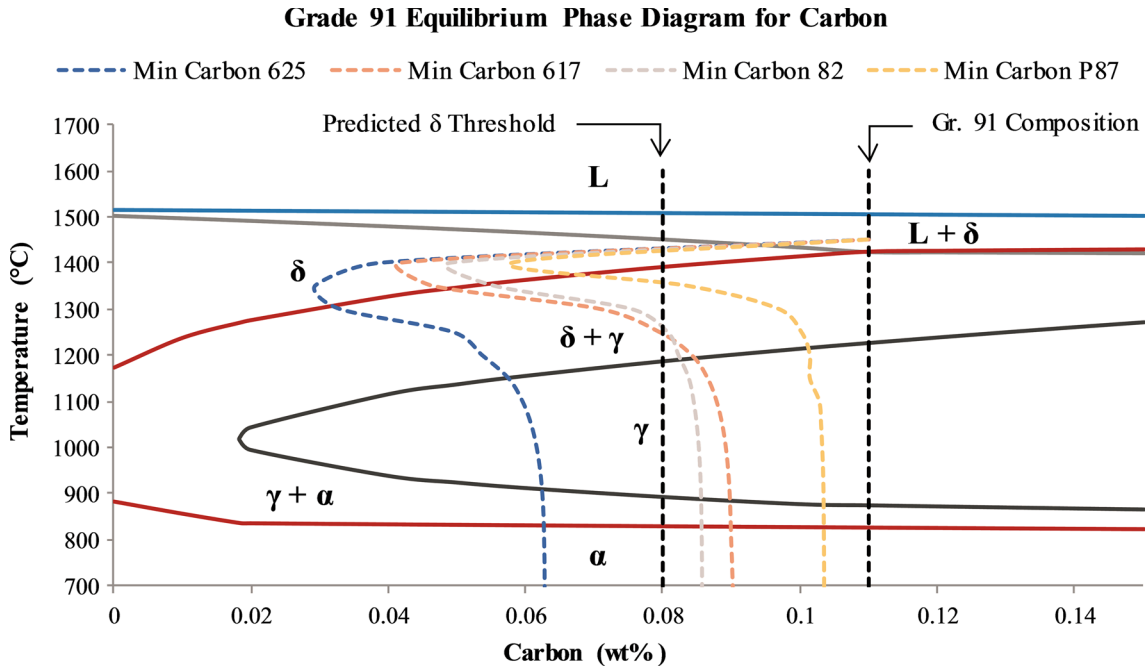

Fig. 18—Equilibrium pseudo-binary phase diagram for carbon in Grade 91 steel including the predicted minimum carbon concentrations for each DMW HAZ as a function of temperature. The average predicted threshold below which retention of δ ferrite was expected was based on Table IX.

Table IX. Critical Carbon Concentration and Level of Carbon Depletion for δ-Ferrite Retention in the Tested Heat of Grade 91 Steel (0.11 Wt Pct Carbon) Based on the Predictions from Referenced Research

References	Maximum Carbon Content for Retention of δ Ferrite, (Wt Pct)	Carbon Depletion for Retention of δ Ferrite, (Wt Pct)
1	0.0762	0.0338
2	0.0788	0.0312
3	0.0855	0.0245
Average	0.0802	0.0298

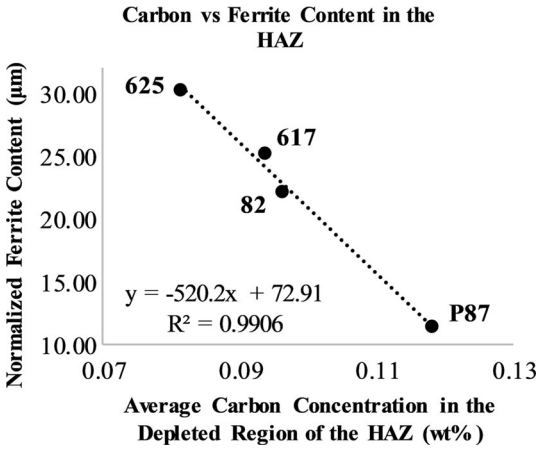

Fig. 19—The measured, normalized ferrite content in the HAZ compared with the predicted carbon content in the diffusion-affected portion of the HAZ for each of the DMWs.

However, a series of experimental evidence has been generated that support the hypothesis of carbon depletion as a controlling mechanism of HAZ δ-ferrite retention in such welds.

The predicted carbon profiles in the DMWs show that carbon depletion in the HAZ would occur within bands approximately 50 μm wide, separated from the phase boundary with local maxima in the carbon content, Figure 15. These predictions correlate well with the HAZ microstructures in the DMWs shown in Figure 8. The width and location of predicted carbon depleted regions coincide with the bands of retained δ ferrite. The local peaks of carbon concentration overlap with narrow bands of fine martensite grains formed between the phase boundary and the δ-ferrite bands. Other than the predicted local enrichment in carbon, slight enrichment in nickel within the band of fine martensite grains was observed in the EPMA scans, Figure 13. The latter can be related to a small amount of alloying elements diffusing across the fusion boundary at high temperatures. Such local enrichment in carbon and nickel stabilized austenite in this region at elevated temperatures, which transformed to martensite on cooling. Because of the low sensitivity and spatial resolution limitations on carbon measurements, the local carbon maxima in the martensite band could not be directly verified.

The EPMA results summarized in Figure 13 and Table VI show that there is no statistical difference in the contents of austenite- and ferrite-stabilizing elements of the martensite and δ-ferrite constituents in the Alloy P87 HAZ. In the statistical comparison of composition using the EPMA line scans, the mean difference interval contained zero, Table VI. With a null hypothesis that the mean difference in the composition of each alloying element was zero, the tests all failed to reject the null hypothesis using a 95 pct confidence index. Therefore, there was no evidence to support that the mean difference for each set of lines was statistically distinct, meaning no indication of a significant change in composition for the measured elements between martensite and δ-ferrite regions.

The hardness maps of the HAZ and fusion zones of Alloy 625 and P87 welds provided additional evidence for HAZ carbon depletion, Figure 11 and Table V. There is a clear indication for statistical differences in the hardness of each weld region and microconstituent measured, which produced two major results. First, the HAZ martensite and the ferrite band martensite had distinct mean hardness values, with the ferrite band martensite being softer. Because the hardness of martensite is directly related to its carbon content, this indicates that the ferrite band was depleted of carbon compared to the rest of the HAZ. Second, the ferrite band martensite was statistically softer for the weld with Alloy 625 than the weld with P87, indicating that the weld with Alloy 625 experienced a greater extent of HAZ carbon depletion. This result was consistent with the trend from the modeling results, Figures 14 and 15, and measured ferrite contents, Table IV, which showed a greater degree of carbon depletion and larger amount of retained δ ferrite in the HAZ of the Alloy 625 weld. These experimental evidences supported the hypothesis that δ-ferrite retention was a result of HAZ carbon depletion and confirmed that the extent of carbon depletion in the HAZ is filler metal specific.

The effect of carbon on the phase balance in Grade 91 is shown in the equilibrium pseudo-binary phase diagram in Figure 18. Based on the experimental results of various studies,[27–31] carbon was identified as the strongest austenite-stabilizing element in Grade 91 steel, where slight carbon depletion would result in δ-ferrite retention in the nonequilibrium cooling conditions of welding. Calculations based on experimentally developed chromium equivalent equations[27–31] show that carbon depletion of approximately 0.03 wt pct, or reduction of the original carbon content from 0.11 to 0.08 wt pct, would result in δ-ferrite retention in the tested heat of Grade 91 steel, Table IX. The predicted temperature dependences of the minimum carbon content in the HAZ of tested DMWs are plotted on Figure 17. In the temperature range of stable δ ferrite, the predicted minimum carbon content varied between 0.029 and 0.04 wt pct, which was below the threshold of 0.08 wt pct, indicating conditions for the retention of δ ferrite in the HAZ of all DMWs.

The effect of carbon on δ-ferrite retention was confirmed by correlating the predicted average carbon content (Figure 17 and Table VIII) to the measured HAZ δ-ferrite content (Table IV) as shown in Figure 19. The strong correlation (R^2 of 0.99) provides a general

validation for the predicted levels of carbon depletion. However, since the actual carbon concentration profile is nearly impossible to measure, the modeling results cannot be verified from a quantitative standpoint. Yet, the correlation is strong enough to validate a linear relationship between the retained δ-ferrite content and the level of carbon depletion in the HAZ. This relationship (Normalized Ferrite Content = $-$ 520.21 $\times$ Average HAZ Carbon Concentration + 72.912) can be used for relative ranking of the level of HAZ carbon depletion in Grade 91 DMWs.

3. *Mechanism of δ-ferrite retention in the HAZ of grade 91 DMWs*

The experimental and modeling results of this study support the following mechanism for retention of δ ferrite in the coarse-grained HAZ of Grade 91 steel during welding with Ni-based filler metals:

1. On heating, the high-temperature HAZ located in front of the moving weld pool undergoes transformation to austenite. Dissolution of $M_{23}C_6$ carbides provides conditions for δ-ferrite nucleation at the austenite grain boundaries. The lower thermal conductivity and higher heat capacity of the Ni-based weld pool extend the dwell time of HAZ at high temperatures, supporting greater degree of carbide dissolution and transformation to δ ferrite.
2. The contact of HAZ with the weld pool, through the fusion boundary and the partially mixed zone, establishes a steep gradient of the carbon chemical potential and a driving force for carbon diffusion toward the fusion zone. Carbon is mixed and diluted within the fusion zone, which maintains the chemical potential gradient.
3. Carbon depletion of the HAZ continues during the solidification process. The release of latent heat of fusion from the nickel-based weld pool slows the cooling rate, which provides additional time for carbon diffusion. The degree of carbon depletion is enhanced by the higher carbon diffusivity in the δ-ferrite phase. The level of carbon depletion becomes sufficient to stabilize a significant portion of the δ-ferrite grains on cooling to room temperature. The retention of δ ferrite is augmented by the fast, nonequilibrium cooling in the HAZ.
4. Toward the end of solidification, reversed diffusion of carbon toward the HAZ may occur, which is controlled by the filler metal composition. A narrow band of δ ferrite grains adjacent to the fusion boundary, which are enriched in carbon and nickel transform back to austenite on cooling.
5. On further cooling, the austenite in HAZ transforms to martensite, resulting in a final martensitic microstructure with a band of retained δ-ferrite grains separated from the phase boundary by a chain of fine martensitic grains.

The proposed mechanism of δ-ferrite retention in the HAZ of Grade 91 steel DMWs with Ni-based filler metals differs from the mechanism of δ-ferrite retention in the fusion zone of Grade 91-matching filler metal welds. The latter is caused by segregation of alloying elements during solidification leading to formation of pockets rich in ferrite-stabilizing elements.[25]

B. *Effect on Mechanical Properties and Service Performance*

Formation of continuous bands of microstructural constituents with composition and properties distinctively different from the rest of the weldment is typical for welds in ferritic and martensitic steels with austenitic filler metals. Formation of such bands, located in parallel or normal to the loading direction, presents a significant concern in terms of structural integrity and service performance of welded joints. Steep gradients in chemical composition, mechanical, and thermophysical properties can result in localized corrosion, strain concentration, loss of strength, brittle crack propagation, and can potentially lead to failures in DMWs in oil and gas, petrochemical, nuclear, and fossil-based power generation systems.

For the discussed case of Grade 91 steel DMW with Ni-based filler metals, the low hardness in the band of retained δ ferrite indicates local softening and lower strength than the surrounding martensitic structure, which may affect the overall strength of the weldment. In addition, as mentioned in the introduction, several studies have linked the presence of δ ferrite to the loss of impact toughness in high chromium martensitic steels and reduction of creep life in creep-resistant steels.[19–23,39]

This study does not provide evidence that the local mechanical properties of the retained δ ferrite have direct influence on the mechanism of premature failures in Grade 91 DMWs, which were recently reported in Reference 16. These failures occur in a region of the partially mixed zone located between the fusion and phase boundaries, which is adjacent to the δ-ferrite band. However, retention of δ ferrite indicated a significant extent of carbon diffusion occurring during welding, and the performed thermodynamic simulations predicted areas of local carbon depletion in the HAZ and enrichment in the partially mixed zone, Figure 13. Since the carbon distribution in these DMWs could not be experimentally validated, its relation to the failure mechanism will be addressed in separate future studies. It can be expected, however, that carbon redistribution in the partially mixed zone would continue during postweld heat treatment and subsequent high-temperature service, and may result in the formation of a carbon-rich zone and precipitation of coarse carbides, which could provide a convenient path for crack propagation.

V. CONCLUSIONS

The results of this study lead to the following conclusions:

- A narrow band of δ-ferrite grains, located parallel to the fusion boundary within the CGHAZ, is retained

in the final microstructure of Grade 91 steel welds made with Ni-based filler metals.

- The mechanism of δ-ferrite retention is based on partial carbon depletion of the CGHAZ during welding. For all the tested DMWs, the predicted levels of carbon depletion were sufficient to stabilize δ ferrite down to room temperature.
- The CGHAZ carbon depletion is caused by solid-state carbon diffusion toward the Ni-based fusion zone. The compositional differences between Grade 91 steel and the Ni-based filler metals generate steep gradients in the carbon chemical potential across the fusion boundary, which serves as a driving force for carbon migration.
- Significant differences the in base metal and filler metal heat capacities and thermal conductivities result in longer dwell times of HAZ at high temperatures, generating favorable conditions for carbon migration across the fusion boundary.
- The extent of carbon depletion and δ-ferrite retention are filler metal specific. Alloy 625 generated the largest extent of carbon depletion and the amount of retained CGHAZ δ ferrite, followed by Alloys 617, 82, and P87 filler metals.
- The retained δ-ferrite content in the CGHAZ of tested DMWs have a strong linear relationship with the predicted levels of carbon depletion. The carbon depletion of CGHAZ resulted in local softening of the martensitic constituent.
- This study did not identify a direct effect of the δ-ferrite retention on the partially mixed zone failures experienced in Grade 91 steel DMWs. However, the soft δ-ferrite band located in the CGHAZ can negatively affect the overall strength, impact toughness, and creep performance of such welds.
- The developed computational model of carbon diffusion in Grade 91 steel DMWs can be applied in studies of carbon behavior during postweld heat treatment and service, and of the potential effect of carbide precipitation and coarsening on the failure mechanism in the partially mixed zone.

REFERENCES

1. F. Masuyama and J.P. Shingledecker: *Proc. Eng.*, 2013, vol. 55, pp. 314–25.
2. K. Maruyama, K. Sawada, and J.I. Koike: *ISIJ Int.*, 2001, vol. 41, pp. 641–53.
3. C. Pan and Z. Zhang: *Mater. Charact.*, 1996, vol. 36, pp. 5–10.
4. J.N. DuPont: *Int. Mater. Rev.*, 2012, vol. 57, pp. 208–34.
5. R. Anand, C. Sudha, T. Karthikeyan, A.L.E. Terrance, S. Saroja, and M. Vijayalakshmi: *J. Mater. Sci.*, 2008, vol. 44, pp. 257–65.
6. R. Anand, C. Sudha, T. Karthikeyan, A.L.E. Terrance, S. Saroja, and M. Vijayalakshmi: *Trans. Indian Inst. Metals*, 2008, vol. 61, pp. 483–486.
7. R. Viswanathan, R. I. Jaffee, and J. Dimmer: *Annual Conference on Materials for Coal Conversion and Utilization (Proceedings),* 1982, pp. 439–70.
8. D. Gandy and K. Coleman, Alternative filler materials for DMWs involving P91 materials, in *EPRI Fifth International Conference—Advances in Materials Technology for Fossil Power Plants*, Marco Island, Fl, 2007, pp. 940–67.
9. J.A. Siefert, J.M. Sanders, J.M. Tanzosh, W.F. Newell, Jr, and J.P. Shingledecker: *Mater. High Temp.*, 2010, vol. 27, pp. 243–52.
10. M.F. Dodge, H.B. Dong, and M.F. Gittos: *Mater. Res. Innov.*, 2014, vol. 18, pp. S4907–S4913.
11. J. Clark: *Ph.D. Dissertation, EFET EngD Centre, UON, Nottingham, UK,* 2015.
12. J. Frei, B.T. Alexandrov, and M. Rethmeier: *Weld. World*, 2016, vol. 60, pp. 459–73.
13. M.K. Samal, M. Seidenfuss, E. Roos, and K. Balani: *Eng. Fail. Anal.*, 2011, vol. 18, pp. 999–1008.
14. B.T. Alexandrov, J.C. Lippold, J.W. Sowards, A.T. Hope, and D.R. Saltzmann: *Weld. World*, 2012, vol. 57, pp. 39–53.
15. G.J. Brentrup, B.S. Snowden, J.N. DuPont, and J.L. Grenestedt: *Weld. J.*, 2012, vol. 91, pp. 252S–259S.
16. Cracking in Thick-Section Dissimilar Metal Welds—Case Studies, EPRI, Palo Alto, CA. 2015.
17. J. Siefert, J. Parker, and T. Totemeier, 2016, p. V005T12A009.
18. M.W. Kuper, B.T. Alexandrov, M.J. Mills, and D.J. Burgess, Dissimilar metal welds in grade 91 steel, in *8th International Conference on Advances in Materials Technology for Fossil Power Plants*, 2016, pp. 1199–1206.
19. B. Gsellmann, D. Halici, B. Krenmayr, C. Poletti, and B. Sonderegger, Thermomechanical investigation of the production process of a creep resistant martensitic steel, in *20th International ESAFORM Conference on Material Forming, ESAFORM 2017*, 2017.
20. P.H.S. Cardoso, C. Kwietniewski, J.P. Porto, A. Reguly, and T.R. Strohaecker: *Mater. Sci. Eng. A*, 2003, vol. 351, pp. 1–8.
21. P. Wang, S.P. Lu, N.M. Xiao, D.Z. Li, and Y.Y. Li: *Mater. Sci. Eng. A*, 2010, vol. 527, pp. 3210–16.
22. D. Carrouge, H.K.D.H. Bhadeshia, and P. Woollin: *Sci. Technol. Weld. Join.*, 2004, vol. 9, pp. 377–89.
23. K. Anderko, L. Schäfer, and E. Materna-Morris: *J. Nucl. Mater.*, 1991, vols. 179–181, pp. 492–95.
24. C. Pandey, M.M. Mahapatra, P. Kumar, and N. Saini: *Mater. Sci. Eng. A*, 2018, vol. 712, pp. 720–37.
25. S. Kobayashi, K. Sawada, T. Hara, H. Kushima, and K. Kimura: *Mater. Sci. Eng. A*, 2014, vol. 592, pp. 241–248.
26. M. L. Santella, R. W. Swindeman, R. W. Reed, and J. M. Tanzosh, Martensite transformation, microsegregation, and creep strength of 9 Cr-1 Mo-V steel weld metal, in *ASM Proceedings of the International Conference: Trends in Welding Research*, 2002, pp. 713–18.
27. S.H. Ryu and J. Yu: *Metall. Mater. Trans. A*, 1998, vol. 29, pp. 1573–78.
28. H. Schneider: *Foundry Trade J.*, 1960, vol. 108, pp. 562–63.
29. F.C. Hull: *Weld. J. (Miami, Fla),* 1973, vol. 52, pp. 193s–203s.
30. M. Tamura, M. Inohara, K. Kusunoki, and Y. Tsuchida: *Jpn. Iron Steel Inst.*, 1984, vol. 70, p. S524.
31. J. Oñoro: *J. Mater. Process. Technol.*, 2006, vol. 180, pp. 137–142.
32. B. Arivazhagan, G. Srinivasan, S.K. Albert, and A.K. Bhaduri: *Fusion Eng. Des.*, 2011, vol. 86, pp. 192–197.
33. N.H. Jung, J.H. Ann, M.J. Lee, N.H. Kang, and K.M. Cho: *J. Korean Inst. Metals Mater.*, 2018, vol. 56, pp. 93–102.
34. J.M. Sosa, D.E. Huber, B. Welk, and H.L. Fraser: *Integr. Mater. Manuf. Innov.*, 2014, vol. 3, p. 10.
35. J.O. Andersson, T. Helander, L. Höglund, P.F. Shi, and B. Sundman: *Calphad*, 2002, vol. 26, pp. 273–312.
36. H. Larsson and L. Höglund: *CALPHAD*, 2009, vol. 33, pp. 495–501.
37. C. Wells, W. Batz, and R. F. Mehl: *Trans. AIME,* 1950, vol. 188.
38. C.A. Wert: *Phys. Rev.*, 1950, vol. 79, pp. 601–05.
39. C. Pandey, M.M. Mahapatra, P. Kumar, N. Saini, J.G. Thakre, R.S. Vidyarthy *et al.*: *Arch. Civil Mech. Eng.*, 2018, vol. 18, pp. 713–722.